RSC Advances

PAPER

View Article Online
View Journal | View Issue

Open Access Article. Published on 28 September 2016. Downloaded on 12/9/2025 4:26:08 AM.
This article is licensed under a Creative Commons Attribution 3.0 Unported Licence.

Cite this: *RSC Adv.*, 2016, **6**, 94539

Facile synthesis of Er^{3+}/Yb^{3+}-codoped $NaYF_4$ nanoparticles: a promising multifunctional upconverting luminescent material for versatile applications†

Peng Du,[a] Laihui Luo*[b] and Jae Su Yu*[a]

Received 7th September 2016
Accepted 28th September 2016

DOI: 10.1039/c6ra22349d

www.rsc.org/advances

The Er^{3+}/Yb^{3+}-codoped $NaYF_4$ upconverting nanoparticles were prepared by a facile hydrothermal method. Under the excitation of 980 nm, the obtained compounds exhibited the featured emissions of Er^{3+} ions. The optical thermometric performance of the Er^{3+}/Yb^{3+}-codoped $NaYF_4$ nanoparticles based on the thermally coupled $^2H_{11/2}$ and $^4S_{3/2}$ levels of Er^{3+} ions in the temperature range of 93–673 K was investigated by the fluorescence intensity ratio technique. The maximum sensitivity was approximately 0.0029 K^{-1}, indicating that both low- and high-temperature detection can be synchronously achieved in Er^{3+}/Yb^{3+}-codoped $NaYF_4$ upconverting nanoparticles. Furthermore, the temperature-dependent emitting color was discussed and it was changed from yellow to red with raising the temperature from 93 to 673 K. In addition, the internal heating properties of the developed nanoparticles caused by laser excitation power were also analyzed. It is found that the temperature of nanoparticles was elevated from 255.03 to 372.03 K with the increment of pump power from 84 to 585 mW. These characteristics suggest that the Er^{3+}/Yb^{3+}-codoped $NaYF_4$ upconverting nanoparticles are a promising candidate for optical temperature sensors and safety signs as well as optical heaters.

1. Introduction

Over the last decades, trivalent lanthanide ions activated upconverting materials in which the near-infrared excitation photons can be converted into visible emissions *via* a multi-photon process have attracted considerable interest because of their versatile applications in cell imaging, cancer therapy, remote optical thermometry, solid-state lighting, and so on.[1–5] Nowadays, erbium (Er^{3+}), as a vital constituent part in lanthanide ions, is intensively studied as the activator for upconverting materials in virtue of its special emissions arising from the intra-4f transitions.[6,7] In general, Er^{3+}-based luminescent materials exhibit two emitting peaks in the green and red regions which are attributed to the ($^2H_{11/2}$, $^4S_{3/2}$) → $^4I_{15/2}$ and $^4F_{9/2}$ → $^4I_{15/2}$ transitions, respectively.[8,9] Nevertheless, owing to the low absorption of the Er^{3+} ions in the infrared region, the Er^{3+} ions single-doped materials usually exhibit dissatisfactory luminescent efficiencies which restrict their applications. Thus, much effort should be made to improve the luminescent efficiency. Fortunately, ytterbium (Yb^{3+}) reveals a strong broad absorption in the infrared region and the energy which is captured from incident photons by Yb^{3+} ions can be easily transferred to Er^{3+} ions, leading to excellent upconversion (UC) luminescent properties in Er^{3+}/Yb^{3+}-codoped materials.[10–13] As a result, the applications of the Er^{3+} ions doped upconverting materials could be extended.

Temperature is a basic and vital parameter in various fields of medical science, industry and daily life, so its detection and monitoring with high accuracy as well as high sensitivity are required. Up to now, the conventional thermometers which are based on the principle of liquid or metal expansion have been widely used in our daily life. However, these traditional thermometers can not satisfy the requirement of medicine and biology, especially, for detecting the temperature distribution of the living cells. Recently, the non-contact optical temperature sensor which is based on the lanthanide ions doped upconverting luminescent materials utilizing the fluorescence intensity ratio (FIR) technique was developed for real-time detection because of its features of high-spatial resolution, high sensitivity and fast response.[14–16] As for the FIR technique, it utilizes the variation of electron transition from two close lying levels (thermally coupled levels) of the lanthanide ions with the elevated temperature. Meanwhile, the energy gap between these two close lying levels should be in the range from 200 to 2000 cm^{-1} to prevent the overlap of two UC emission bands and to allow the upper excited

[a]Department of Electronics and Radio Engineering, Kyung Hee University, Yongin 446-701, Republic of Korea. E-mail: jsyu@khu.ac.kr; Fax: +82 31 201 3820; Tel: +82 31 206 2820

[b]Department of Microelectronic Science and Engineering, Ningbo University, 315211 Ningbo, China. E-mail: luolaihui@nbu.edu.cn

† Electronic supplementary information (ESI) available. See DOI: 10.1039/c6ra22349d

Open Access Article. Published on 28 September 2016. Downloaded on 12/9/2025 4:26:08 AM.
This article is licensed under a Creative Commons Attribution 3.0 Unported Licence.

level to possess a minimum population.[17–19] Currently, the temperature sensing properties of the Er^{3+}-based upconverting materials have been extensively investigated owing to its featured green UC emissions from the thermally coupled levels ($^2H_{11/2}$, $^4S_{3/2}$) to the ground state ($^4I_{15/2}$) as well as the appropriate energy separation.[20,21] According to previous reports,[22–24] one knows that most of the Er^{3+}-based optical temperature sensors can only be operated in either high temperature or low temperature circumstance, demonstrating that the low- and high-temperature monitoring can not be synchronously carried out in these optical thermal probes. To solve this problem, developing a temperature sensor which can be operated in a broad temperature range including low and high temperatures is required.

In this work, we chose the sodium yttrium fluoride ($NaYF_4$) as the luminescent host because of its low phonon energy (around 362 cm^{-1}) which helps to decrease the possibility of the non-radiative (NR) transition and to enhance the UC luminescent efficiency,[25,26] and the Er^{3+}/Yb^{3+}-codoped $NaYF_4$ nanoparticles were fabricated by means of a hydrothermal route. The phase composition, microstructure and room-temperature UC emission performance of the prepared nanoparticles were analyzed. Meanwhile, on the basis of FIR technique, the temperature-dependent UC emission spectra were recorded to investigate the temperature sensing properties. In addition, to explore the potential application of the obtained nanoparticles as an optical heater, the internal heating performance which is induced by the laser excitation power was detailedly studied by analyzing the pump power-dependent UC emission spectra.

2. Experimental

2.1 Synthesis of Er^{3+}/Yb^{3+}-codoped $NaYF_4$ nanoparticles

The hydrothermal method was applied to synthesize the Er^{3+}/Yb^{3+}-codoped $NaYF_4$ (abbreviated as: $NaYF_4$:Er^{3+}/Yb^{3+}; here, the concentrations of Er^{3+} and Yb^{3+} were 2 and 20 mol%, respectively) nanoparticles.[1] The raw materials, such as sodium fluoride (NaF; 99%), yttrium(III) nitrate hexahydrate ($Y(NO_3)_3\cdot 6H_2O$; 99.8%), erbium(III) nitrate pentahydrate ($Er(NO_3)_3\cdot 5H_2O$; 99.9%), ytterbium(III) nitrate pentahydrate ($Yb(NO_3)_3\cdot 5H_2O$; 99.9%) and oleic alcohol, were purchased from Sigma-Aldrich. In a typical route, 0.6 g NaOH was first weighted and dissolved in 3 mL de-ionized (DI) water. Meanwhile, 10 mL oleic alcohol and 20 mL ethanol was added into the above mixture. Then the mixed solution was vigorously agitated until it became transparent. Subsequently, 1.56 mmol $Y(NO_3)_3\cdot 6H_2O$ (0.5 M), 0.04 mmol $Er(NO_3)_3\cdot 5H_2O$ (0.5 M), 0.4 mmol $Yb(NO_3)_3\cdot 5H_2O$ (0.5 M) and 8 mmol NaF (1 M) were slowly dropped into the former solution. The homogenous gelatinous mixture was then transferred into a 100 mL stainless steel autoclave after 30 min agitation. After that, the system was sealed and heated at 200 °C for 10 h. The final product was washed by DI water and ethanol for several times, and dried at 80 °C for 6 h in the air.

2.2 Characterization

The X-ray diffraction (XRD) measurement was carried out by using a X-ray diffractometer (Bruker D8 Advance) with Cu Kα radiation (λ = 1.54046 Å) to identify the crystal structure of synthesized nanoparticles. The particle size and microstructure properties of the obtained products were examined by using a field-emission scanning electron microscope (FE-SEM) (LEO SUPPA 55, Carl Zeiss) and transmission electron microscope (TEM) (JEM-2100F, JEOL) equipped with energy dispersive X-ray spectrum (EDS). For the UC emission measurement, a 980 nm diode laser was employed as the incident light source and the UC emission spectrum was recorded by using a spectrofluorometer (FS5). Under the excitation of 980 nm with the pump power of 84 mW, the temperature-dependent UC emission spectra were measured by FS5 and the temperature from 93 to 673 K was adjusted *via* a temperature controlled system (Linkam HFS600E-PB2).

3. Results and discussion

3.1 Phase composition and morphology properties

In order to explore the phase composition of the fabricated upconverting nanoparticles, the XRD pattern of the $NaYF_4$:Er^{3+}/Yb^{3+} nanoparticles was measured. As presented in Fig. S1,† the XRD pattern revealed that most of the diffraction peaks were well indexed to the hexagonal phase of the $NaYF_4$ (JCPDS#16-0334), while there also existed several weak diffraction peaks corresponding to the cubic phase of $NaYF_4$ (JCPDS#06-0342). The unit cell structures of the $NaYF_4$ with hexagonal and cubic phases are shown in Fig. 1(b) and (c), respectively. To better analyze the crystal structure of the obtained nanoparticles, the Rietveld refinement was carried out by utilizing a General Structure Analysis System (GSAS) software and the corresponding profile is displayed in Fig. 1. The lattice parameters and the reliability factors are summarized in Table S1.† The reliability factors of refinement were R_p = 9.38%, R_{wp} = 12.58% and χ^2 = 0.891, demonstrating that the quality of the refinement was receivable. Furthermore, on the basis of the XRD refinement, the $NaYF_4$:Er^{3+}/Yb^{3+} nanoparticles possessed the lattice parameters of $a = b$ = 5.932823 (Å), c = 3.482378 (Å) and unit cell volume V = 106.152 (Å^3), as shown in Table S1,† which were slightly smaller than that of the pure hexagonal $NaYF_4$ ($a = b$ = 5.96 Å, c = 3.53 Å and V = 125.39 Å^3) because the larger-sized Y^{3+} (0.9 Å) ions were replaced by the smaller-sized Er^{3+} (0.89 Å) and Yb^{3+} (0.868 Å) ions.

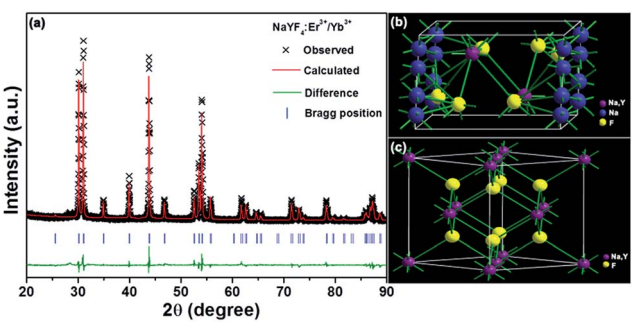

Fig. 1 (a) Rietveld XRD refinement for the $NaYF_4$:Er^{3+}/Yb^{3+} nanoparticles. (b and c) Schematic presentation of the hexagonal and cubic structure of $NaYF_4$, respectively.

This journal is © The Royal Society of Chemistry 2016

Open Access Article. Published on 28 September 2016. Downloaded on 12/9/2025 4:26:08 AM.
This article is licensed under a Creative Commons Attribution 3.0 Unported Licence.

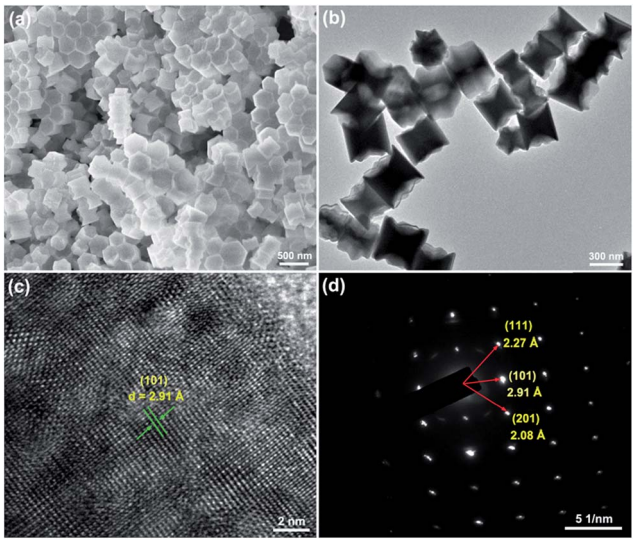

Fig. 2 (a) FE-SEM image, (b) TEM image, (c) HR-TEM image and (d) SAED pattern of the $NaYF_4$:Er^{3+}/Yb^{3+} nanoparticles.

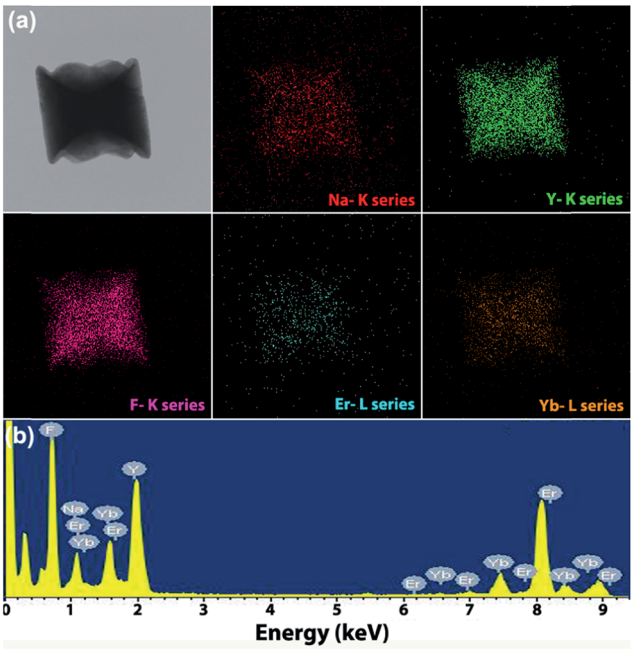

Fig. 3 (a) Elemental mappings and (b) EDS spectrum of the $NaYF_4$:Er^{3+}/Yb^{3+} nanoparticles.

The FE-SEM and TEM analyses were employed to observe the microstructure and particle size of the resultant samples. The FE-SEM image, as shown in Fig. 2(a), confirmed that the as-prepared compounds consisted of uniformly hexagonal nanoprisms. The average diameter of these hexagonal nanoprisms was determined to be about 419 nm and the length was approximately 370 nm. The TEM image (Fig. 2(b)) further revealed the uniform nanoparticles with the shape of hexagonal prism matched well with the aforementioned FE-SEM result. As demonstrated in Fig. 2(c), the high-resolution TEM (HR-TEM) image presented clear lattice fringes and the interplanar spacing was estimated to be around 2.91 Å which is close to the *d*-spacing value of (101) plane of hexagonal $NaYF_4$. The selected area electron diffraction (SAED) pattern suggested that the obtained nanoparticles were of single crystalline in nature (see Fig. 2(d)). The elemental mappings revealed that the constituent elements (Na, Y, F, Er and Yb) were homogeneously distributed in the region of the nanoparticles, as depicted in Fig. 3(a). Fig. 3(b) shows the EDS spectrum of the $NaYF_4$:Er^{3+}/Yb^{3+} nanoparticles. The presence of the pattern peaks of Na, Y, F, Er and Yb in the EDS spectrum indicated the formation of the Er^{3+}/Yb^{3+}-codoped $NaYF_4$ nanoparticles.

3.2 Room-temperature UC emissions and energy level diagram

To evaluate the UC luminescence properties of the $NaYF_4$:Er^{3+}/Yb^{3+} nanoparticles, the UC emission spectrum was measured at room temperature under the excitation of 980 nm laser diode with the fixed pump power of 84 mW. As shown in Fig. 4, the UC emission spectrum was dominated by an intense red emission centered at around 662 nm which is assigned to the $^4F_{9/2} \rightarrow {}^4I_{15/2}$ transition along with two green emissions at 523 and 542 nm due to the $^2H_{11/2} \rightarrow {}^4I_{15/2}$ and $^4S_{3/2} \rightarrow {}^4I_{15/2}$ transitions of Er^{3+} ions, respectively.[27–29] Meanwhile, a weak blue emission located at around 490 nm ($^4F_{7/2} \rightarrow {}^4I_{15/2}$) was also detected (see Fig. 4).[30]

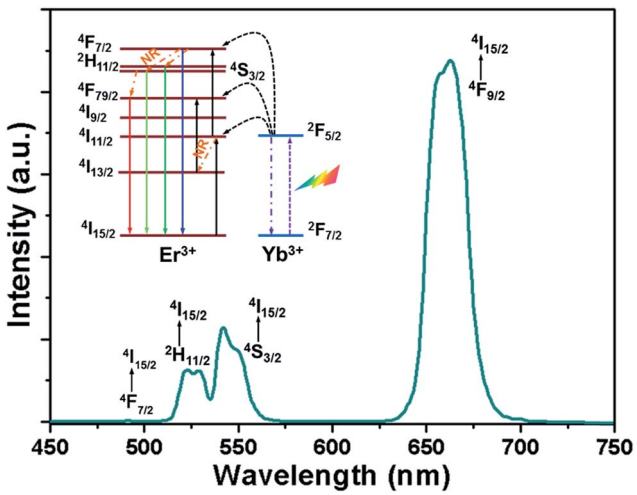

Fig. 4 Room-temperature UC emission spectrum of the $NaYF_4$:Er^{3+}/Yb^{3+} nanoparticles excited under 980 nm light with the pump power of 84 mW. Inset shows the simplified energy level diagram of Er^{3+} and Yb^{3+} ions.

The simplified energy level diagram of Er^{3+} and Yb^{3+} ions, which was employed to expound the UC mechanism for the generation of the characteristic emissions of Er^{3+} ions, is depicted in the inset of Fig. 4. As demonstrated in the energy level diagram, the incident photons are first captured by the Yb^{3+} ions, and then the electrons in the ground state, $^2F_{7/2}$, are pumped to the excited state of $^2F_{5/2}$. Due to the superior energy level overlap between the Yb^{3+} and Er^{3+} ions, an efficient ET would arise from the Yb^{3+} ions to the adjacent Er^{3+} ions, *i.e.*, Yb^{3+} ($^2F_{5/2}$) + Er^{3+} ($^4I_{15/2}$) → Yb^{3+} ($^2F_{7/2}$) + Er^{3+} ($^4I_{11/2}$), leading to the population of the $^4I_{11/2}$ level of

Open Access Article. Published on 28 September 2016. Downloaded on 12/9/2025 4:26:08 AM.
This article is licensed under a Creative Commons Attribution 3.0 Unported Licence.

Er^{3+} ions. Meanwhile, the $^4F_{7/2}$ level will be populated from the $^4I_{11/2}$ level either by directly absorbing an incident photon or a second ET from Yb^{3+} to Er^{3+} ions (Yb^{3+} ($^2F_{5/2}$) + Er^{3+} ($^4I_{11/2}$) → Yb^{3+} ($^2F_{7/2}$) + Er^{3+} ($^4F_{7/2}$)). Subsequently, the majority of electrons in the $^4F_{7/2}$ level nonradiatively decay to the $^2H_{11/2}$ and $^4S_{3/2}$ levels. As a result, the blue and green emissions are generated because of the radiative transition processes, namely, $^4F_{7/2}$ → $^4I_{15/2}$, $^2H_{11/2}$ → $^4I_{15/2}$ and $^4S_{3/2}$ → $^4I_{15/2}$. For the intense red emission, there exist two routes to populate the $^4F_{9/2}$ level. As presented in the inset of Fig. 4, part of the electrons in the $^4I_{11/2}$ level can nonradiatively relax to the $^4I_{13/2}$ level, and these electrons can be further excited to the $^4F_{9/2}$ level through an efficient ET from Yb^{3+} to Er^{3+} ions (Yb^{3+} ($^2F_{5/2}$) + Er^{3+} ($^4I_{13/2}$) → Yb^{3+} ($^2F_{7/2}$) + Er^{3+} ($^4F_{9/2}$)). In addition, the nonradiative (NR) transition from the $^4S_{3/2}$ level can also contribute to the population of the $^4F_{9/2}$ level. Owing to these efficient processes, bright red emission corresponding to the $^4F_{9/2}$ → $^4I_{15/2}$ transition was achieved.

3.3 Temperature sensing properties

On the basis of the UC emission spectrum (Fig. 4), one knows that the energy separation between the $^2H_{11/2}$ and $^4S_{3/2}$ levels was about 607.3 cm^{-1} (19 nm) which makes the $^2H_{11/2}$ level to be populated from the $^4S_{3/2}$ level by thermal excitation, leading to the variation in the FIR values of the green emissions from the ($^2H_{11/2}$, $^4S_{3/2}$) → $^4I_{15/2}$ transitions of Er^{3+} ions at the elevated temperature. Therefore, the non-contact temperature thermometry is expected to be realized in Er^{3+} ions doped luminescent materials by the FIR technique. In order to explore the suitability of the obtained nanoparticles for applications in optical temperature sensor, the dependence of UC emissions on temperature was recorded. Fig. 5 shows the green UC emission spectra (normalized at the emission band of 542 nm) of the $NaYF_4$:Er^{3+}/Yb^{3+} nanoparticles with the varied temperature from 93 to 673 K. As depicted in Fig. 5, the positions of the emission peaks hardly changed with increasing the temperature, whereas the UC emission intensity from the $^2H_{11/2}$ level showed a gradually rising tendency compared to that from the $^4S_{3/2}$ level. The FIR values of the green UC emissions arising from the $^2H_{11/2}$ → $^4I_{15/2}$ and $^4S_{3/2}$ → $^4I_{15/2}$ transitions were calculated as presented in Fig. 6(a). Clearly, the FIR value varied from 0.275 to 1.657 with increasing the temperature from 93 to 673 K. According to the Boltzmann distribution theory and by ignoring the effects from self-absorption of emissions, the FIR from two thermally coupled levels can be defined as:[15,31,32]

$$\mathrm{FIR} = \frac{I_H}{I_S} = \frac{N(H)}{N(S)} = A\exp\left(\frac{-\Delta E}{kT}\right) + B, \quad (1)$$

where I_H and I_S are the integrated luminescent emission intensities for the $^2H_{11/2}$ → $^4I_{15/2}$ and $^4S_{3/2}$ → $^4I_{15/2}$ transitions of Er^{3+} ions, respectively. N(H) and N(S) represent the population number of the $^2H_{11/2}$ and $^4S_{3/2}$ levels, respectively. ΔE is the energy gap between the $^2H_{11/2}$ and $^4S_{3/2}$ levels. k is the Boltzmann constant. T is the absolute temperature. A and B are the constants. Through analyzing the experimental data with the help of eqn (1), the coefficients A and B were found to be 4.039 and 0.319, respectively, and the energy gap between the thermally coupled levels of $^2H_{11/2}$ and $^4S_{3/2}$ was $\Delta E \sim 519.9$ cm^{-1} which is close to the value obtained from the UC emission spectrum.

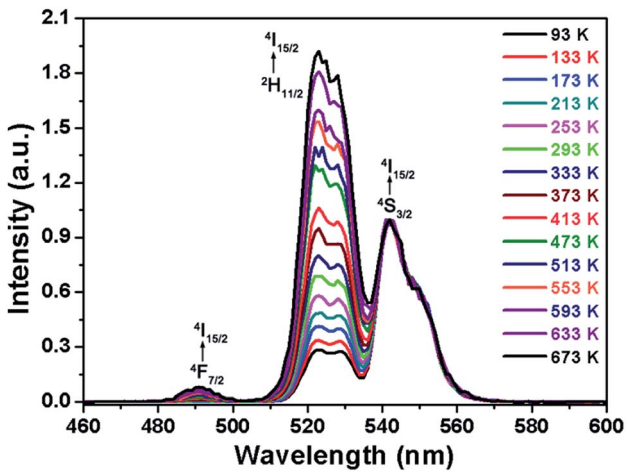

Fig. 5 Normalized green UC emission spectra of the $NaYF_4$:Er^{3+}/Yb^{3+} nanoparticles with different temperatures ranging from 93 to 673 K.

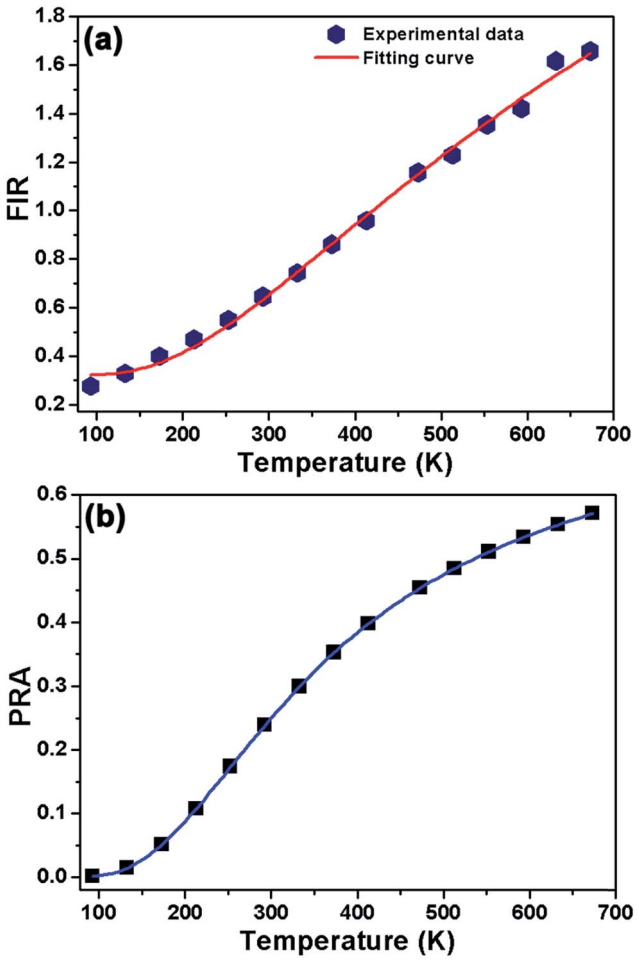

Fig. 6 (a) Temperature-dependent FIR values of I_H/I_S for the $NaYF_4$:Er^{3+}/Yb^{3+} nanoparticles. (b) Temperature-dependent PRA values of the $^2H_{11/2}$ and $^4S_{3/2}$ thermal coupled levels.

This journal is © The Royal Society of Chemistry 2016

Open Access Article. Published on 28 September 2016. Downloaded on 12/9/2025 4:26:08 AM.
This article is licensed under a Creative Commons Attribution 3.0 Unported Licence.

For the aforementioned channel to obtain the temperature-induced population redistribution, the temperature-dependent population redistribution ability (PRA) is given by the following expression:[33,34]

$$\mathrm{PRA} = \frac{I_{\mathrm{U}}}{I_{\mathrm{U}+I_{\mathrm{L}}}} = \frac{I_{\mathrm{H}}}{I_{\mathrm{H}} + I_{\mathrm{S}}}, \quad (2)$$

where I_{U} and I_{L} are the integrated luminescent emission intensities from the upper and lower thermally coupled levels to ground sate, respectively. I_{H} and I_{S} possess the same meaning as described in eqn (1). Combined with eqn (1) and (2), the PRA can be approximately rewritten as:

$$\mathrm{PRA} \approx \frac{A}{A + \exp(\Delta E/kT)}, \quad (3)$$

where A, ΔE, k and T exhibit the same meaning as presented in eqn (1). In present work, according to the above fitting result, one obtains that the values of A and ΔE were 4.039 and 519.9 cm^{-1}, respectively. The temperature-dependent PRA of $^2\mathrm{H}_{11/2}$ and $^4\mathrm{S}_{3/2}$ thermally coupled levels was estimated as depicted in Fig. 6(b). It is evident that the PRA value can be significant affected by the absolution temperature. When the temperature was 93 K, the PRA value was as low as 0.0013. Nevertheless, with elevating the temperature, the value of PRA increased rapidly, reaching its maximum value of about 0.5706 when the temperature was 673 K, suggesting that the population between the $^2\mathrm{H}_{11/2}$ and $^4\mathrm{S}_{3/2}$ levels can be prominently affected by the external temperature. Therefore, the $NaYF_4:Er^{3+}/Yb^{3+}$ nanoparticles were expected to show superior temperature sensing properties.

To apprehend the sensing ability of the synthesized nanoparticles, it is necessary to investigate the sensor sensitivity. As we know, the relative sensor sensitivity is the rate of FIR changes in response to the change of absolute temperature and it can be expressed:[35–37]

$$S = \frac{\mathrm{d}R}{\mathrm{d}T} = \left[A \exp\left(\frac{-\Delta E}{kT}\right)\right] \frac{\Delta E}{kT^2}. \quad (4)$$

By means of eqn (4), the relative sensitivity as a function of absolution temperature was estimated, as can be seen in Fig. 7. The $NaYF_4:Er^{3+}/Yb^{3+}$ nanoparticles can be worked in the temperature range of 93–673 K and the maximum sensitivity was approximately 0.0029 K^{-1} at the temperature of 368 K. Furthermore, the sensitivity was slightly changed at higher temperature and the sensitivity was around 0.0022 K^{-1} when the temperature was 673 K. In compare with other Er^{3+}/Yb^{3+}-coactivated upconverting luminescent materials, like oxides, tungsten-tellurite glasses, ceramics, sulfides and fluoride nanoparticles, for temperature thermometry, as demonstrated in Table 1, a satisfied result was obtained in the $NaYF_4:Er^{3+}/Yb^{3+}$ nanoparticles. Different with other temperature sensing materials in which only the high temperature thermometry was available, the $NaYF_4:Er^{3+}/Yb^{3+}$ nanoparticles possessed a broad operating temperature range from 93 to 673 K. In addition, the present sensitivity obtained from the $NaYF_4:Er^{3+}/Yb^{3+}$ nanoparticles was also comparable with other fluoride-based temperature sensors (see Table 1). These characteristics make the $NaYF_4:Er^{3+}/Yb^{3+}$ nanoparticles suitable for optical temperature sensor applications.

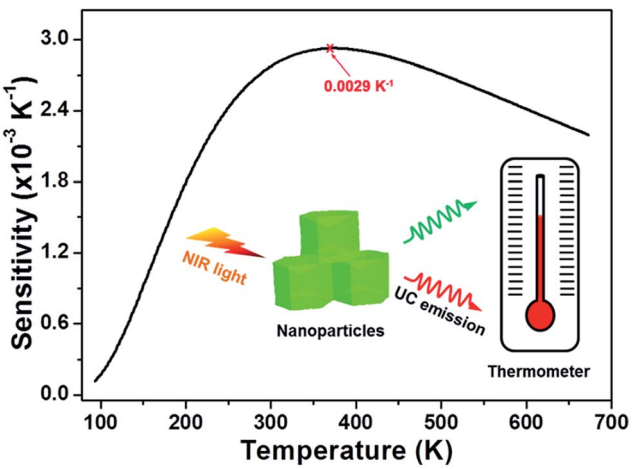

Fig. 7 Relative sensor sensitivity as a function of temperature for the $NaYF_4:Er^{3+}/Yb^{3+}$ nanoparticles.

3.4 Temperature-dependent CIE chromaticity coordinates

From the temperature-dependent UC emission spectra of the $NaYF_4:Er^{3+}/Yb^{3+}$ nanoparticles, as described in Fig. S2,† both the green and red emission intensities exhibited a declining

Table 1 Temperature range and maximum sensitivity of Er^{3+} ions doped compounds

Compounds	Temperature (K)	Sensitivity (K^{-1})	Excitation wavelength (nm)	References
$CaWO_4:Er^{3+}/Yb^{3+}$	300–540	0.0025	980	39
$BaTiO_3:Er^{3+}/Yb^{3+}$	120–505	0.0019	980	40
$Gd_2O_3:Er^{3+}/Yb^{3+}$	300–900	0.0039	980	41
TeO_2-$WO_3:Er^{3+}/Yb^{3+}$	300–690	0.0028	980	42
$La_2O_2S:Er^{3+}/Yb^{3+}$	300–573	0.0080	980	43
$La_2S_3:Er^{3+}/Yb^{3+}$	293–900	0.0075	971	44
$NaYF_4:Er^{3+}/Yb^{3+}/Gd^{3+}/Nd^{3+}$	288–328	0.0026	976	45
$NaLuF_4:Er^{3+}/Yb^{3+}$	303–523	0.0052	980	46
β-$NaGdF_4:Er^{3+}/Yb^{3+}$	303–563	0.0037	980	47
$NaYF_4:Er^{3+}/Yb^{3+}$	93–673	0.0029	980	Present work

Open Access Article. Published on 28 September 2016. Downloaded on 12/9/2025 4:26:08 AM.
This article is licensed under a Creative Commons Attribution 3.0 Unported Licence.

tendency with the elevated temperature which was assigned to the thermal quenching effect. As is known, the NR transition possibility for the multiphonon relaxation can be expressed as:[26,38]

$$W_{NR}(T) = W_{NR}(0)[1 - \exp(-h\nu/kT)]^{-\Delta E/kT}, \quad (5)$$

where $W_{NR}(T)$ and $W_{NR}(0)$ stand for the NR relaxation probability at the temperature of T and $T = 0$ K, respectively, $h\nu$ is the phonon energy, k is the Boltzmann coefficient, T is the temperature and ΔE is the energy separation involved. Clearly, the $W_{NR}(T)$ value is proportional to temperature, namely, the higher temperature contributes to the larger $W_{NR}(T)$ value. Thus, when the temperature was increased, the quenching of the luminescent emission intensity was caused. As presented in the inset of Fig. S2,† the emission intensity ratio of red to green emissions (I_R/I_G) was enhanced with the increment of temperature, indicating that color-controllable emissions could be realized in the $NaYF_4:Er^{3+}/Yb^{3+}$ nanoparticles by properly adjusting the temperature. From the UC emission spectra, the CIE chromaticity coordinates of the $NaYF_4:Er^{3+}/Yb^{3+}$ nanoparticles as a function of temperature were calculated and the corresponding results are depicted in Fig. 8 and Table S2.† It is evident that the emitting color of the synthesized nanoparticles was shifted from yellow to red with controlling the temperature from 93 to 673 K (see Fig. 8). These multicolor emissions further confirmed that the emission intensity ratio of I_R/I_G trended to increase with raising the temperature which matched well with the result presented in the inset of Fig. S2.† The temperature-induced multicolor emission properties suggested that the $NaYF_4:Er^{3+}/Yb^{3+}$ nanoparticles may also have promising applications in high-temperature environment as a safety sign apart from the temperature sensor.

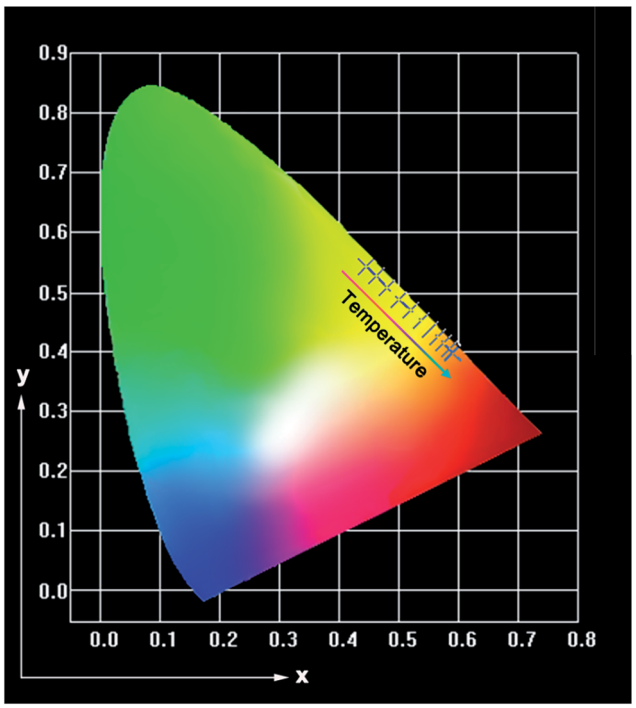

Fig. 8 CIE chromaticity coordinates of the $NaYF_4:Er^{3+}/Yb^{3+}$ nanoparticles at different temperatures.

3.5 Optical heating ability

As is known, whenever the RE ions activated materials are exposed to the incident light source, a small portion of the incident photons absorbed by the optical materials will be converted into heat through the NR relaxation route. Consequently, the temperature of the product will be increased. This characteristic makes the luminescent materials appropriate for optical heaters. For the purpose of analyzing the thermal effect induced by the laser excitation, the pump power-dependent UC emission spectra were examined. The normalized green UC emission spectra of the $NaYF_4:Er^{3+}/Yb^{3+}$ nanoparticles at the different pump powers of 84–585 mW are illustrated in the inset of Fig. 9 and the corresponding FIR values are calculated, as listed in Table S3.† Clearly, the FIR value varied from 0.534 to 0.860 with the increased pump power from 84 to 585 mW. From the aforementioned FIR technique, one obtains that an exact FIR value stands for a special temperature. Therefore, the internal heating performance of the host lattice induced by laser could be evaluated by rewriting eqn (1) and the temperature (T) can be calculated through the following formula:

$$T = \left[\frac{1}{\ln A - \ln(R - B)}\right]\frac{\Delta E}{k}, \quad (6)$$

where the A, B and ΔE values were determined to be approximately 4.039, 0.319 and 519.9 cm^{-1}, respectively. On the basis of eqn (6), the temperature of the $NaYF_4:Er^{3+}/Yb^{3+}$ nanoparticles as a function of pump power was calculated. It is clear that the temperature exhibited an increasing tendency with raising the pump power and the maximum value was around 372.03 K when the pump power was 585 mW (see Fig. 9 and Table S3†), confirming that the $NaYF_4:Er^{3+}/Yb^{3+}$ nanoparticles possessed the capability of converting the incident photons (laser excitation power) into heat. As a result, the $NaYF_4:Er^{3+}/Yb^{3+}$ nanoparticles were promising candidates as optical heaters.

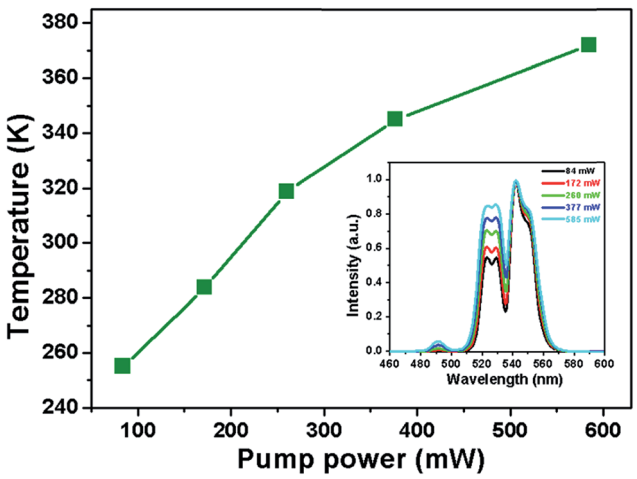

Fig. 9 Sample temperature as a function of pump power. Inset depicts the normalized green UC emission spectra of the $NaYF_4:Er^{3+}/Yb^{3+}$ nanoparticles with different pump powers.

This journal is © The Royal Society of Chemistry 2016

Open Access Article. Published on 28 September 2016. Downloaded on 12/9/2025 4:26:08 AM.
This article is licensed under a Creative Commons Attribution 3.0 Unported Licence.

4. Conclusions

In summary, the highly efficient Er^{3+}/Yb^{3+}-codoped $NaYF_4$ upconverting nanoparticles were synthesized by a facile hydrothermal approach. The visible UC emission peaks situated at about 490, 523, 542 and 662 nm, which originated from the intra-4f transitions of Er^{3+} ions, were observed when excited at 980 nm of near-infrared light. The optical thermometric properties of the $NaYF_4$:Er^{3+}/Yb^{3+} nanoparticles in the temperature range of 93–673 K were studied *via* utilizing the FIR technique of two green UC emissions from two thermally coupled levels of $^2H_{11/2}$ and $^4S_{3/2}$. The maximum sensitivity was found to be around 0.0029 K^{-1} at 368 K. Furthermore, the emitting color of the as-prepared nanoparticles was tuned from yellow to red with the increased absolute temperature from 93 to 673 K. Additionally, through theoretical calculation, the laser excitation power-induced thermal effect was investigated and the temperature of nanoparticles varied from 255.03 to 372.03 K with the increase of pump power from 84 to 585 mW. These results demonstrated that the $NaYF_4$:Er^{3+}/Yb^{3+} nanoparticles are promising multifunctional upconverting luminescent materials for noninvasive temperature thermometry, optical heater and safety sign for high-temperature circumstance.

Acknowledgements

This work was supported by the National Research Foundation of Korea (NRF) Grant funded by the Korea government (MSIP) (No. 2015R1A5A1037656).

Notes and references

1 Z. Yi, X. Li, Z. Xue, X. Liang, W. Lu, H. Peng, H. Liu, S. Zeng and J. Hao, *Adv. Funct. Mater.*, 2015, **25**, 7119–7129.
2 L. Cheng, C. Wang and Z. Liu, *Nanoscale*, 2013, **5**, 23–37.
3 D. Gao, D. Tian, G. Xiao, B. Chong, G. Yu and Q. Pang, *Opt. Lett.*, 2015, **40**, 3580–3583.
4 Y. Zhong, I. Rostami, Z. Wang, H. Dai and Z. Hu, *Adv. Mater.*, 2015, **27**, 6418–6422.
5 Y. Tian, Y. Tian, P. Huang, L. Wang, Q. Shi and C. Cui, *Chem. Eng. J.*, 2016, **297**, 26–34.
6 S. Zhao, W. Liu, X. Xue, Y. Yang, Z. Zhao, Y. Wang and B. Zhou, *RSC Adv.*, 2016, **6**, 81542–81551.
7 P. Du, L. Luo, W. Li and Q. Yue, *J. Appl. Phys.*, 2014, **116**, 014102.
8 X. Huang, *Opt. Mater. Express*, 2016, **6**, 2165–2176.
9 S. S. Perera and F. A. Rabuffetti, *CrystEngComm*, 2016, **18**, 5818–5825.
10 D. He, C. Guo, S. Zhou, L. Zhang, Z. Yang, C. Duan and M. Yin, *CrystEngComm*, 2015, **17**, 7745–7753.
11 X. Huang and J. Lin, *J. Mater. Chem. C*, 2015, **3**, 7652–7657.
12 F. Wang, Y. Han, C. S. Lim, Y. Lu, J. Wang, J. Xu, H. Chen, C. Zhang, M. Hong and X. Liu, *Nature*, 2010, **463**, 1061–1065.
13 W. Bian, Y. Qi, W. Lu, X. Yu, X. Xu and J. Qiu, *CrystEngComm*, 2016, **18**, 2642–2649.
14 Z. Zhang, C. Guo, H. Suo, X. Zhao, N. Zhang and T. Li, *Phys. Chem. Chem. Phys.*, 2016, **18**, 18828–18834.
15 X. Wang, Q. Liu, Y. Bu, C. Liu, T. Liu and X. Yan, *RSC Adv.*, 2015, **5**, 86219–86236.
16 A. K. Soni, A. Kumari and V. K. Rai, *Sens. Actuators, B*, 2015, **216**, 64–71.
17 K. Zheng, Z. Liu, C. Lv and W. Qin, *J. Mater. Chem. C*, 2013, **1**, 5502–5507.
18 A. Pandey, V. K. Rai, V. Kumar, V. Kumar and H. C. Swart, *Sens. Actuators, B*, 2015, **209**, 352–358.
19 H. Suo, C. Guo, Z. Yang, S. Zhou, C. Duan and M. Yin, *J. Chem. Mater. C*, 2015, **3**, 7379–7385.
20 P. Du, L. Luo, W. Li, Q. Yue and H. Chen, *Appl. Phys. Lett.*, 2014, **104**, 152902.
21 H. Zhang, D. Peng, W. Wang, L. Dong and C. Pan, *J. Phys. Chem. C*, 2015, **119**, 28136–28142.
22 S. Liu, D. Chen, Z. Wan, Y. Zhou, P. Huang and Z. Ji, *RSC Adv.*, 2016, **6**, 71176–71187.
23 V. Lojpur, G. Nikolić and M. D. Dramićanin, *J. Appl. Phys.*, 2014, **115**, 203106.
24 S. F. León-Luis, V. Monteseguro, U. R. Rodríguez-Mendoza, M. Rathaiah, V. Venkatramu, A. D. Lozano-Gorrín, R. Valiente, A. Muñoz and V. Lavín, *RSC Adv.*, 2014, **4**, 57691–57701.
25 J. Shan, M. Uddi, N. Yao and Y. Ju, *Adv. Funct. Mater.*, 2010, **20**, 3530–3537.
26 G. Chen, H. Liu, H. Liang, G. Somesfalean and Z. Zhang, *J. Phys. Chem. C*, 2008, **112**, 12030–12036.
27 D. Gao, X. Zhang and W. Gao, *ACS Appl. Mater. Interfaces*, 2013, **5**, 9732–9739.
28 D. Gao, D. Tian, X. Zhang and W. Gao, *Sci. Rep.*, 2016, **6**, 22433.
29 P. Du, L. Luo, H. Park and J. S. Yu, *Chem. Eng. J.*, 2016, **306**, 840–848.
30 L. Huang, X. Liu, W. Xu, B. Chen and J. Lin, *J. Appl. Phys.*, 2001, **90**, 5550–5553.
31 P. Du, L. Luo and J. S. Yu, *J. Alloys Compd.*, 2015, **632**, 73–77.
32 W. Xu, H. Zhao, Y. Li, L. Zheng, Z. Zhang and W. Cao, *Sens. Actuators, B*, 2013, **188**, 1096–1100.
33 X. Wang, J. Zheng, Y. Xuan and X. Yan, *Opt. Express*, 2013, **21**, 21596–21606.
34 X. Wang, C. Liu and X. Yan, *RSC Adv.*, 2014, **4**, 24170–24175.
35 L. H. Fischer, G. S. Harms and O. S. Wolfbeis, *Angew. Chem., Int. Ed*, 2011, **50**, 4546–4551.
36 F. Huang, Y. Gao, J. Zhou, J. Xu and Y. Wang, *J. Alloys Compd.*, 2015, **639**, 325–329.
37 P. Du, L. Luo, Q. Yue and W. Li, *Mater. Lett.*, 2015, **143**, 209–211.
38 L. A. Riseberg and H. W. Moos, *Phys. Rev.*, 1968, **174**, 429–438.
39 X. Cheng, K. Yang, J. Wang, L. Yang and X. Cheng, *Opt. Mater.*, 2016, **58**, 449–453.
40 M. K. Mahata, T. Koppe, T. Mondal, C. Brüsewitz, K. Kumar, V. K. Rai, H. Hofsäss and U. Vetter, *Phys. Chem. Chem. Phys.*, 2015, **17**, 20741–20753.
41 B. Tian, B. Chen, Y. Tian, X. Li, J. Zhang, J. Sun, S. Fu, H. Zhong, X. Zhang, H. Yu and R. Hua, *Mater. Express*, 2013, **3**, 241–246.

42 A. Pandey, S. Som, V. Kumar, V. Kumar, K. Kumar, V. K. Rai and H. C. Swart, *Sens. Actuators, B*, 2014, **202**, 1305–1312.
43 Y. Yang, C. Mi, F. Yu, X. Su, C. Guo, G. Li, J. Zhang, L. Liu, Y. Liu and X. Li, *Ceram. Int.*, 2014, **40**, 9875–9880.
44 Y. Yang, C. Mi, F. Jiao, X. Su, X. Li, L. Liu, J. Zhang, F. Yu, Y. Liu and Y. Mai, *J. Am. Ceram. Soc.*, 2014, **97**, 1769–1775.
45 D. T. Klier and N. U. Kumke, *RSC Adv.*, 2015, **5**, 67149–67156.
46 K. Zheng, W. Song, G. He, Z. Yuan and W. Qin, *Opt. Express*, 2015, **23**, 7653–7658.
47 D. Chen, Z. Wan, Y. Zhou, P. Huang, J. Zhong, M. Ding, W. Xiang, X. Liang and Z. Ji, *J. Alloys Compd.*, 2015, **638**, 21–28.

Open Access Article. Published on 28 September 2016. Downloaded on 12/9/2025 4:26:08 AM.
This article is licensed under a Creative Commons Attribution 3.0 Unported Licence.

This journal is © The Royal Society of Chemistry 2016